nature communications

Article

https://doi.org/10.1038/s41467-024-52841-1

Comfortable wearable thermoelectric generator with high output power

Received: 12 March 2024

Accepted: 23 September 2024

Published online: 02 October 2024

Check for updates

Lei Miao[1,7] ✉, Sijing Zhu[1,2,7], Chengyan Liu[3], Jie Gao[3], Zhongwei Zhang[1], Ying Peng[4], Jun-Liang Chen[3], Yangfan Gao[3], Jisheng Liang[1] & Takao Mori[5,6] ✉

Wearable thermoelectric generators provide a reliable power generation method for self-powered wearable electronic devices. However, there has been a lack of research regarding the comfort of wearable thermoelectric generators. Here we propose a design for a comfortable wearable thermoelectric generators system with high output power based on sandwiched thermoelectric model. This model paves the way for simultaneously optimizing comfort (skin temperature and pressure perception) and output power by systematically considering a variety of thermal resistive environments and bending states, the properties of the thermoelectric and encapsulation materials, and the device structure. To verify this strategy, we fabricate wearable thermoelectric generators using Mg-based thermoelectric materials. These materials have great potential for replacing traditional Bi_2Te_3-based materials and enable our wearable thermoelectric generators with a power density of 18.4 μWcm^{-2} under a wearing pressure of 0.8 kPa and with a skin temperature of 33 °C, ensuring the wearer's comfort.

Rapid progress in personalization propelled by remarkable advancements in wearable and implantable electronics is revolutionizing the field of healthcare[1,2]. An uninterrupted power supply is indispensable for such bioelectronics, particularly for life-critical applications like artificial cardiac pacemakers. Wearable thermoelectric generators (w-TEGs) can provide continuous electrical energy by harnessing human body heat through the Seebeck effect[3–5]. Their numerous advantages, including high reliability, the absence of moving parts and noise, and environmental friendliness, make them an ideal potential solution for ensuring uninterrupted power[6–10]. Despite these benefits, however, research into achieving high-output and comfortable w-TEGs is still in its infancy.

To ensure wearability, w-TEGs must be comfortable, including maintaining appropriate skin temperature, limiting perceived pressure, and being mechanically flexible (including bending, stretching, and folding) to accommodate the body's dynamic movement[11,12]. While significant progress has been achieved in elevating the output power of w-TEGs at extreme conditions[13–18], their comfort, unfortunately, remains consistently overlooked, even though this is indeed a necessary consideration for applications since it affects the stability of the heat source and the wearability of the device, like for other wearable electronics[19,20].

Optimizing both wearability and device output presents a significant challenge. Wearability (the device's bending stiffness and bending radius, the body's perceived temperature, etc.) and output

[1]Guangxi Key Laboratory for Relativity Astrophysics, Guangxi Novel Battery Materials Research Center of Engineering Technology, State Key Laboratory of Featured Metal Materials and Life-cycle Safety for Composite Structures, School of Physical Science and Technology, Guangxi University, Nanning, P. R. China. [2]School of Mechanical and Electrical Engineering, Guilin University of Electronic Technology, Guilin, P. R. China. [3]Guangxi Key Laboratory of Information Materials, Engineering Research Center of Electronic Information Materials and Devices, Ministry of Education, Guilin University of Electronic Technology, Guilin, P. R. China. [4]Guilin University of Electronic Technology, Guilin, P. R. China. [5]Research Center for Materials Nanoarchitectonics (MANA), National Institute for Materials Science (NIMS), Tsukuba, Japan. [6]Graduate School of Pure and Applied Sciences, University of Tsukuba, Tsukuba, Ibaraki, Japan. [7]These authors contributed equally: Lei Miao, Sijing Zhu. ✉e-mail: miaolei@gxu.edu.cn; mori.takao@nims.go.jp

performance (power density:P_d, load resistance:R_l, voltage density:V_d, etc.) are intricately coupled through the device structure, the properties of the thermoelectric (TE) material, and the environment[21–23]. Hence, achieving comfort and high output simultaneously is not straightforward. In essence, maximizing output does not rely only on optimizing TE material performance, but also requires meticulous design of the w-TEG's structure and thermal management at the system level. However, no general analytical formula for system efficiency and wearability of w-TEGs has been reported to date.

In this study, we establish a model for w-TEGs utilizing a sandwiched structure, the most representative of TE devices. By integrating mechanical and TE analyses, we derive explicit formulas to quantitatively analyze the optimization of multidimensional parameters for both comfort and power output while worn on a human body in real-world environments. We establish a direct link between the system's output and its wearing comfort by considering the interconnections among the structural parameters of the device, the performance of the TE materials, and the external environment. We identify the optimal structural matching range for maximizing system efficiency and wearability and predict the maximum output power of w-TEGs positioned at various locations on or near the human body. Moreover, experimental validation is conducted on actual human subjects using w-TEGs that employ n-type Mg_3Bi_2 and *p*-type MgAgSb-based TE materials (*n*-type: $Mg_{3.2}Bi_{1.49}Sb_{0.5}Se_{0.01}$; p-type: $MgAg_{0.95}Sb_{0.99}$; the TE performance of each is shown in Supplementary Fig. S1). Recently, these materials have been intensively studied for use in non-wearable TEGs due to their cost effectiveness and high TE performance near room temperature[24,25]. The outcomes here closely approximate those for state-of-the-art Bi_2Te_3-based w-TEGs, highlighting the potential of our fabricated w-TEGs. Our work provides a comprehensive strategy for the design of w-TEG systems, incorporating a multidimensional quantification analysis to maximize device output power while ensuring wearing comfort.

Result

Design process for w-TEGs

Coupled interactions among the thermal networks in w-TEGs and their low in-plane thermal conductivity resulting from the use of flexible substrates give rise to additional thermal leakage in these devices[15,26]. Finite element analysis (FEA), in which all influencing factors, including lateral heat transfer analysis and parameters related to TE leg shape, are encompassed within a unified model, has proven to be an effective approach for addressing such intricate issues[27–29]. Nevertheless, its computational cost is notably high, and it cannot offer concise and profound guidance similar to that from analytical formulas, making it challenging to analyze coupling mechanisms and quantify parameters from a macroscopic perspective. One-dimensional (1D) numerical analysis is straightforward and efficient[30,31]. It is often employed for general, macroscopic mechanism quantification, aiding in parameter guidance for w-TEG design.

Here we have proposed a complete design strategy based on the 1D coupling mechanism. Figure 1 illustrates the logical framework for the full parameter optimization of a wearable TE power generation module based on the coupled field equations of TE and mechanical models. Our design strategy takes into account various application scenarios by considering environmental temperature (T_a), bending radius (r), body temperature (T_b), and parameters of the TE and encapsulation materials, including Young's modulus (E) and thermal conductivity (κ_E) values for the encapsulation materials. Here the encapsulation materials are defined as the filler and substrates of the w-TEG. For a given environment and set of materials, the output and wearability of the system are highly dependent on the TE leg geometry and the heat dissipation design[32–34]. We first established the connection between the wearability parameters for the system, including skin pressure (Pr) and skin temperature (T_s), and those for its structure, including length (L)/width (w) of the TE leg, the fill factor (F), the *p*-/*n*-type material area ratio ($F_{p/n}$), the ambient and total heat transfer coefficient (h_a,h), and obtained the ranges of values for the structural parameters. Then, on the base of ensuring wearability, the optimal geometric parameters of the TE leg were obtained by combining multiple parameters and optimizing the output efficiency of the system. When determining optimal geometric parameters that meet the design requirements, the properties of the TE and encapsulation materials must also be properly considered since, on the one hand, the TE materials directly determine the electrical and thermal performance of the w-TEG system under ideal conditions, while on the other hand, its mechanical performance mainly depends on the physical properties of the encapsulation materials. For example, using low-E filling materials for the TE legs or the absence of filling materials can greatly improve the flexibility of the device but reduce its reliability. The device design should thus be based on the application environment and incorporate matching encapsulation materials. After the optimal geometric parameters were obtained, FEA was used for more precise adjustment to maximize the power output while meeting the wearing resistance requirements for any given material and environmental conditions and the device was finally prepared for experimental verification.

Coupling mechanism between output performance and wearing comfort

To assess the various aspects of w-TEG system performance, we have separately constructed thermal-electric and mechanical models of the device when worn on a human body as ideally simulated (no displacement between the two materials, without considering the centerline stretching and without considering Poisson's ratio, etc.). The thermal-electric model primarily focuses on investigating the w-TEG's output performance and T_s, while the mechanical model is employed to study the flexibility of the w-TEG and determine the minimum pressure exerted on the skin when worn. The mechanical model is shown in Fig. 2a, b and assumes a cylindrical shape for the body part on which the w-TEG is worn. According to static equilibrium principles, given its three-layer structure, the bending stiffness (Ei_{TEG}) of the system should satisfy the following expression (see Supplementary Note S1):

$$Ei_{TEG} = E_b^* i_b + E^* i + E_t^* i_t \tag{1}$$

In this context, E_b^*, E^*, and E_t^* represent the effective Young's modulus of the bottom substrate (hot side of TEG), the filler layer, and the top substrate (cold side of TEG), respectively, and are functions of the material's Young's modulus and F. i_b, i, and i_t denote the respective area moments of inertia of the bottom substrate, the filler layer, and the top substrate with respect to the neutral axis and are functions of the material's style modulus and L (see Supplementary Notes S1, S2). $E_b^* i_b$, $E^* i$, and $E_t^* i_t$ represent the effective bending stiffness of the bottom substrate, the filler layer, and the top substrate, respectively. Thus, given Young's modulus and height of the material, the device's Ei_{TEG} with respect to the F and L can be computed. Furthermore, as shown in Fig. 2b, it is possible to derive the pressure (Pr) exerted on the skin as a result of the device bending against a body part (assumed to be an ideal cylinder), and this can be expressed as (see Supplementary Notes S1, S2):

$$Pr = \frac{12Ei_{TEG}}{W_{TEG}{}^3\left(\sqrt[2]{r^2 - 0.25W_{TEG}{}^2} + r^2 - 0.25\frac{W_{TEG}{}^2}{r}\right)}, \tag{2}$$

where W_{TEG} is the width of the TEG and r is the bending radius. Equation (2) is based on the encapsulation material being a linear

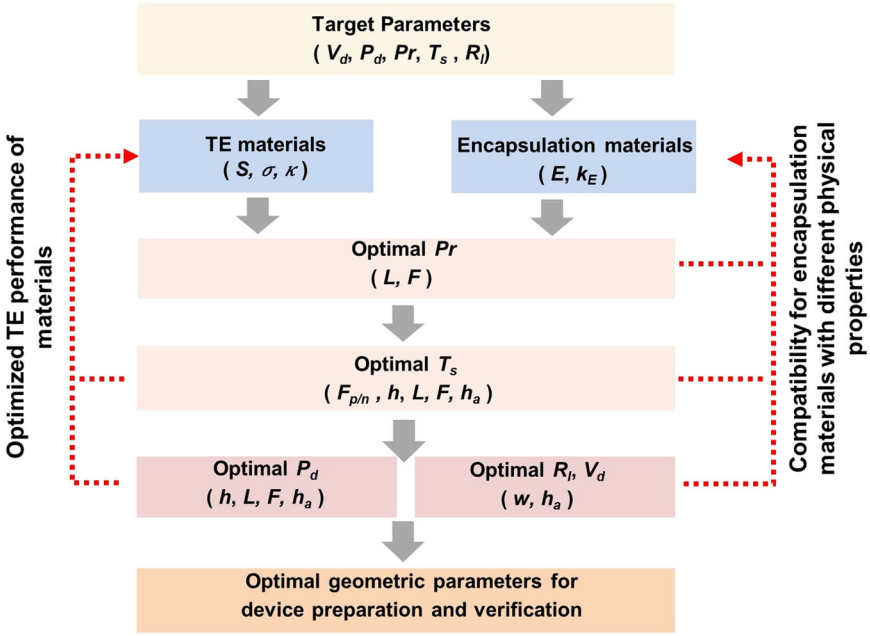

Fig. 1 | Logical framework for the full-parameter optimization of a w-TEG. The target parameters (V_d, P_d, Pr , T_s, R_l) are determined by the application environment, the optimized process, and optimal geometric parameters for w-TEG preparation and performance verification.

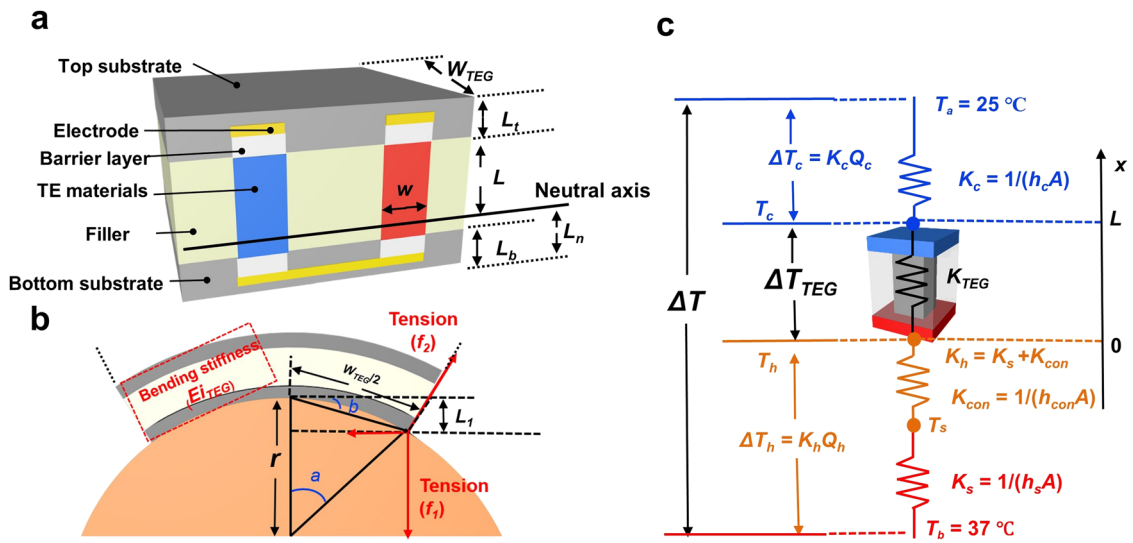

Fig. 2 | w-TEG models. a Schematic illustration of the internal structure of the w-TEG. **b** Mechanical model of the w-TEG during bending. **c** Thermal network of the w-TEG system.

elastomer. For the hyperelastomer material, we also give the derivation process (Mooney_Rivlin model, see Supplementary Note S3), but the result is more complicated. For general applications, we can approximate the linear elastomer to simplify the analysis (It adapts to the application environment when the bending radius exceeds 5 cm.).

The thermal-electric model, the parameters for which are depicted in Fig. 2c, integrates core body temperature, the thermal resistance of the skin layers (K_s), contact thermal resistance between the device and the skin (K_{con}), the TE module, and heat sink elements to evaluate device output and T_s. Generally, human skin is a complex, multi-layered system. Skin temperature varies depending on the ambient temperature or different points of the body (Supplementary Table S1). To simplify the calculations, the core body temperature was set within the range of 36.5 °C to 37.5 °C, which is according to balancing the energy produced through metabolism with the heat dissipated to the environment through convection, radiation and evaporation processes, and is typically independent of the environment[9,35]. Since T_s exhibits relatively minor variations within a small range around room temperature[36,37], we model it using an equivalent heat transfer coefficient (Supplementary Table S2). In accordance with non-equilibrium thermodynamics, under 1D current and energy flow conditions, the differential equations describing the temperature distribution $T(x)$ in the presence of electric current density J_e are:

$$\nabla(\kappa \cdot \nabla T) + \frac{J_e^2}{\sigma} - \tau \cdot J_e \cdot \nabla T = 0 \tag{3}$$

$$Q = S \cdot T \cdot J_e - \kappa \cdot \nabla T \tag{4}$$

where S, σ, κ, T, τ, and Q represent the Seebeck coefficient, electrical conductivity, thermal conductivity, temperature, Thomson coefficient, and heat flux, respectively. In practical w-TEG systems, the filler

material significantly impacts both heat transfer and output. Therefore, we incorporate the study of filler thermal conductivity into our thermodynamic model. For simplicity, we naturally assume that the contribution of the filler material to heat conduction within the TE system is uniform. Under this assumption, and by disregarding the Thomson effect and the contact resistance and thermal resistance of the substrate (see Supplementary Note S4), the governing equations and boundary conditions for a single-leg TE system under steady-state conditions are as follows:

$$\kappa^* \frac{d^2T}{dx^2} + \frac{R_{TEG}I^2}{LAF} = 0, \tag{5}$$

$$-\kappa^* A\frac{dT}{dx} + ST_hI = Q_h = \frac{T_b - T_h}{K_h}, x = L, \tag{6}$$

and

$$-\kappa^* A\frac{dT}{dx} + ST_cI = Q_c = \frac{T_c - T_a}{K_c}, x = 0, \tag{7}$$

where I, A, and R_{TEG} are the electric current, cross-sectional area, and resistance, respectively, of the TE leg; T_a and T_b are ambient temperature and body temperature, respectively; T_c and T_h are the temperature at the cold and hot sides, respectively, of the TEG; Q_c and Q_h are the heat flow values at the cold and hot sides, respectively, of the TEG; and K_c and K_h are the thermal resistance values at the cold and hot sides, respectively, of the TEG. κ^* represents the thermal conductivity of the TEG, encompassing that for both the TE legs and the filler material. It can be expressed by the following formula:

$$\kappa^* = \kappa F + \kappa_f(1 - F), \tag{8}$$

where κ and κ_f are the thermal conductivity values for the TE materials and the filler materials, respectively. The derived expressions for the simplified generator's maximum power density (P_d) and the effective temperature difference shown below are presented in detail in Supplementary Note S4:

$$P_d = \frac{\Delta T^2}{4} \times \frac{Z}{\left(1 + \frac{\kappa^*}{hL}\right)^2 \cdot \frac{L}{F\kappa} + \left(\frac{\kappa^*}{Lh} + 1\right) \cdot \frac{ZT_{avg}}{h}} \tag{9}$$

and

$$\frac{1}{h} = \frac{1}{h_c} + \frac{1}{h_{con}} + \frac{1}{h_s}, \tag{10}$$

where $Z = S^2\sigma/\kappa$; ZT_{avg} is the average TE figure of merit determining the efficiency of TEG[38,39]. h_c, h_s, and h_{con} are the heat transfer coefficients for the cold side of the TEG, the skin, and the contact between the TEG and the skin, respectively. Through analysis of the P_d, it can be deduced that attaining high P_d requires a multifaceted approach. On one hand, it involves enhancing the ΔT, h, and ZT while decreasing κ_f. On the other hand, achieving optimal structural design, which includes optimizing L and F along with κ, is essential for achieving maximum power output.

While the pursuit of high P_d is undoubtedly a primary objective for real-world applications of w-TEGs, it comes with the trade-off of increased L, which could impact wearing comfort. Here we also focused on T_s as a quantitative reference for wearing comfort. Assuming that the w-TEG operates at the optimal current, and considering the heat transfer equation, the expression of T_s is:

$$T_s = T_b - \frac{K_s}{K}\Delta T = T_b - \frac{\Delta T}{\frac{h_s}{h} + \frac{h_s L}{\kappa F + \kappa_f(1-F)}}, \tag{11}$$

where K is the total thermal resistance of the system and can be expressed as: $K = K_c + K_h + K_{TEG}$. K_{TEG} is the total thermal resistance of the TEG. The above analysis is based on a single-leg model (*i.e.*, the TE properties of the p- and n-type materials are identical), and we also analyzed a two-leg model (Supplementary Note S5). Once the TE materials are identified, the optimal cross-sectional area ratio ($F_{p/n,\ opt}$) for the *p*- and *n*-type materials can be obtained by inserting the structural parameters into Supplementary Eq. (S57). Notably, under conditions where the temperature difference is not significant and the TE performance of the materials remains stable, the optimal $F_{p/n,\ opt}$ for achieving the highest P_d does not change with variations in device structure or heat dissipation (Supplementary Fig. S5a–c). The equivalent ZT and effective thermal conductivity can then be derived [Supplementary Eqs. (S61) and (S63) and Fig. S5d]. Once the equivalent ZT (ZT_{pn}) and effective thermal conductivity (κ_{pn}) are determined, they can be incorporated into the single-leg model for analysis.

Multi-parameter w-TEG optimization

Based on the study of the above model, the object-oriented w-TEG design is determined by the usable temperature difference, bending radius, equivalent skin thermal resistance, area, target power, and voltage density of w-TEGs by considering the application environment of the target use. In addition, the appropriate TE materials need to be selected according to the temperature range, and flexible, low-thermal-conductivity fillers and high-thermal-conductivity substrates need to be selected according to the application. Here we chose Mg-based TE materials for our study. Compared to the state-of-the-art room-temperature Bi_2Te_3 and Ag_2Se alloys, Mg-based materials are much more cost-effective since they contain no expensive elements and they are less toxic, making them better suited for wearable devices, as well as the most promising candidates to replace Bi_2Te_3 for room-temperature applications[15,24,40–43]. In addition, to ensure uniform heat dissipation and mechanical performance during bending when the device is worn, we employed a high-thermal-conductivity and stretchable liquid metal (LM)-metal-encapsulated polydimethylsiloxane (PDMS/LM/Copper, E_b&E_t = 820 kPa, $\kappa_1 = 2.1\ Wm^{-1}K^{-1}$) for the substrate. The intermediate fill material comprises a soft and low-thermal-conductivity polyurethane foam (E = 270 kPa, $\kappa_f = 0.025\ Wm^{-1}K^{-1}$). We first considered the mechanical properties as the optimization parameters for the w-TEG. Figure 3a shows Pr as a function of device structure on the arm (r = 5 cm). Evidently, the Pr of the w-TEG increases with increasing L and F. The black line represents the critical Pr (0.5 to 0.8 kPa) associated with wearing tight-fitting clothing on the body[44]. Beyond this Pr, the skin perceives tightness. Results for the T_s of the arm were determined based on Eq. (11) and are shown as a function of structure at room temperature in Fig. 3b. Here, we set the operative environment to the arm, with an equivalent skin heat transfer coefficient of 30 $Wm^{-2}K^{-1}$ and a contact heat transfer coefficient of 80 $Wm^{-2}K^{-1}$ between the device and the skin. These values are used as references and are based on previous studies, although they will vary in practical applications due to the presence of sweat discharge[45,46]. In addition, the heat transfer coefficient of the cold end is set to 30 $Wm^{-2}K^{-1}$. Clearly, as F increases or L decreases, the T_s decreases accordingly. We defined four temperature ranges to represent the perception of warmth or coldness on the skin. For instance, temperatures exceeding 34 °C are perceived as hot, and those between 32 and 34 °C are perceived as warm, which is considered ideal for comfort. Temperatures between 32 and 30 °C and below 30 °C are perceived as cold and very cold, respectively. It is worth noting that temperature perception varies among individuals and body parts. For example,

https://doi.org/10.1038/s41467-024-52841-1

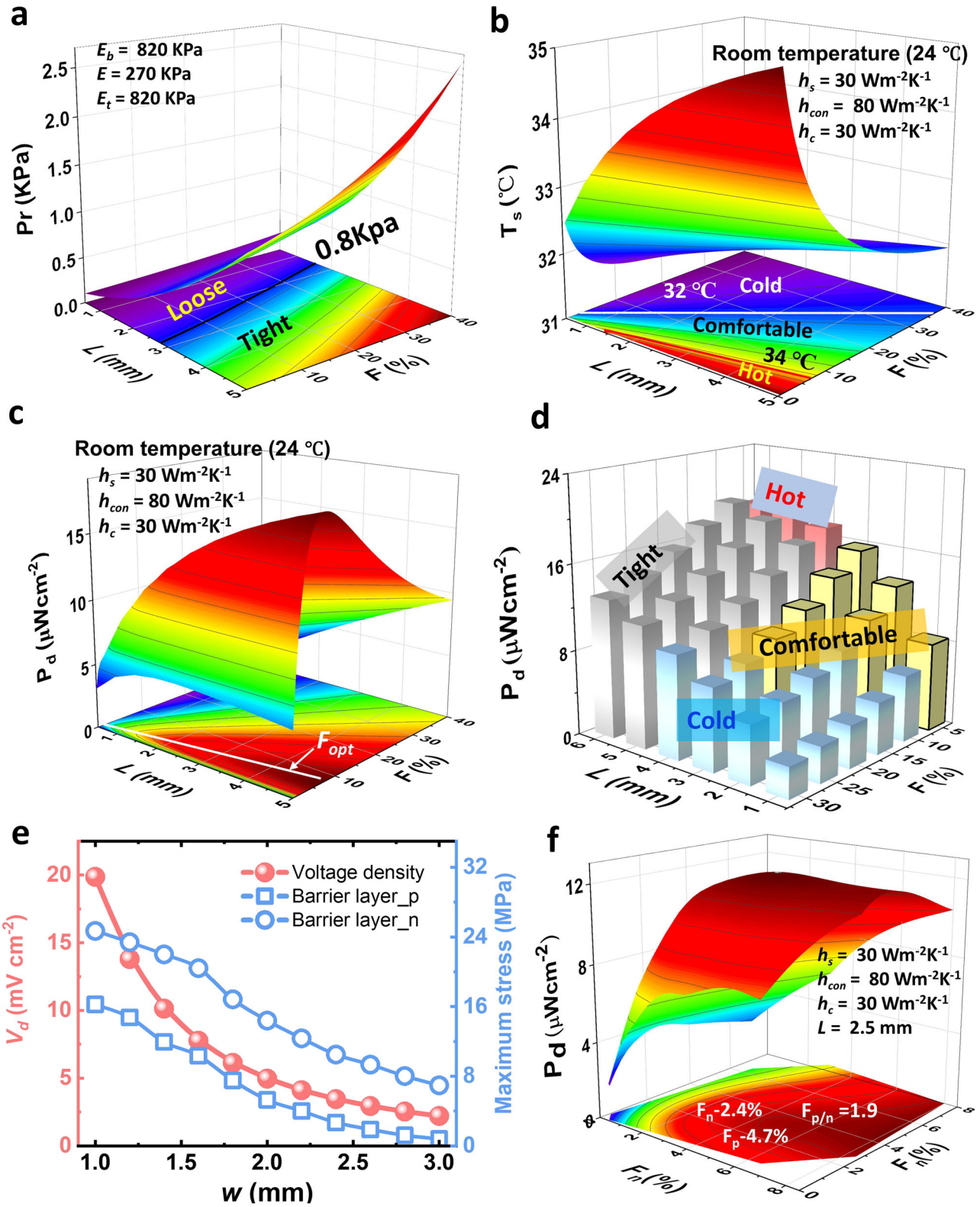

Fig. 3 | Structural design workflow for a w-TEG system. a–c *Pr*, T_s, and P_d, respectively, as functions of *F* and *L* for a device designed for the arm at room temperature. **d**, Relationship among the w-TEG's P_d and T_s and Pr based on (**a**–**c**). **e** Voltage density and maximum stress as functions of *w*. **f** Final refinement and optimization through FEA.

lower-temperatures objects are perceived differently on the head and feet. Our definition of warmth and coldness perception is based on the examples of the torso and the arms for reference. After the w-TEG wearing comfort was optimized, to maximize P_d, it was determined as a function of the structure using Eq. (9), and the results are shown in Fig. 3c. On one hand, increasing *L* can improve the output, and on the other hand, when *L* is fixed, the filling factor needs to meet certain conditions to maximize the

power output. Generally, given the selection of TE materials, the thermal conductivity remains constant. Thus, Eq. (9) can be reformulated to obtain the optimal expression for F:

$$F_{opt} = \frac{\sqrt[2]{(\kappa - \kappa_f) \cdot (\kappa - \kappa_f + Z \cdot T_{avg} \cdot \kappa)}}{(\kappa - \kappa_f)^2 + (\kappa^2 - \kappa \cdot \kappa_f) \cdot Z \cdot T_{avg}} \times (h \cdot L + \kappa_f) \quad (12)$$

For ease of analysis, mapping the structural parameters yields the coupled results for Pr, T_s, and output P_d when the w-TEG is worn on the arm, as illustrated in Fig. 3d. While higher temperature differences, TE leg performance, and heat transfer coefficients lead to elevated output, it is essential to maintain them within a reasonable range to ensure long-term wearing comfort, a criterion to which wearable devices should adhere. High P_d is undoubtedly appealing. However, as device flexibility diminishes, it subjects the skin to increased pressure. In this case, a TE leg height greater than 3 mm would result in reduced flexibility or excessively high T_s. Conversely, reducing the device height too much to enhance flexibility would be inappropriate as well since the resulting increased F may lead to a sensation of coldness on the skin. For long-term wear, prioritizing wearing comfort over device output enhancement is the design objective we aspire to achieve. As shown in Supplementary Fig. S6, achieving comfort-centric structural device design becomes particularly stringent under low-temperature conditions with high heat transfer.

In addition to P_d, output voltage density (V_d) is another crucial indicator that should be considered throughout the comprehensive design process. The expression for output voltage density under maximum power output conditions depends not only on the structural parameters discussed above but also significantly on the TE leg width (w, Supplementary Note S6):

$$V_d = \frac{1}{2} \frac{\Delta T S F_{opt} L h}{w^2 \left(L h + \kappa F_{opt} + \kappa_f (1 - F_{opt}) \right)} \quad (13)$$

The derived V_d results are displayed in Fig. 3e, which shows that the voltage density can reach high values when the w is very small. In regard to the w, a comprehensive balance among factors such as manufacturing precision, material mechanical strength, and welding strength should be considered for device design. For example, FEA (see Supplementary Fig. S7 for details) shows that thinner TE legs are subjected to greater shear stress than thicker TE legs (Fig. 3e) and are, therefore, more likely to break. It should be noted that the above analysis disregards secondary thermal effects within the TEG system, including the thermal diffusion resistance within the substrate and the contact thermal resistance between the filler and the TE leg, which are challenging to incorporate into 1D numerical analysis. Furthermore, w does not contribute to the P_d in the 1D numerical analysis, but in real-world applications, the influence of secondary thermal effects will also impact the P_d. A smaller w leads to a more even distribution of thermal conduction, reducing the impact of secondary thermal effects and aligning more closely with the estimations from the 1D numerical analysis, which was validated through more accurate FEA (see Supplementary Fig. S8 for details). Based on the research discussed above, certain parameter margins should be reserved (Supplementary Fig. S9 shows P_d based on different models as a function of F, h, w. The margin can be reserved according to the related parameters.). When finalizing the design structure, allow for minor adjustments using FEA, as illustrated in Fig. 3f, and in turn, for greater precision among these parameters.

Furthermore, at $F = F_{opt}$, P_d increases with increasing L and h (Supplementary Fig. S12a, b). For given target P_d and ambient temperature values, the range of heat transfer and L values satisfying the target power can be determined by using Eqs. (8–10, 12). The device structure can then be optimized to satisfy the target power as much as possible while simultaneously improving the wearability of the device using Eqs. (2, 8–13) (the detailed design process is shown in Supplementary Fig. S12–S14). Whether under low or high heat dissipation conditions, the optimal L exceeds 8 mm (Supplementary Fig. S15a, b). While reducing the κ of the TE material contributes slightly to increasing P_d and decreasing the optimal L (Supplementary Fig. S15c, d), its effect is rather minor. This finding differs from the conclusions of Suarez et al., primarily due to the absence of an optimized structural design in their studies[35,47]. In our study, for w-TEG based on inorganic bulk TE materials (usually the thermal conductivity of TE materials exceeds 0.1 $Wm^{-1}K^{-1}$), assuming that ZT is unchanged, reducing κ of TE materials (while the power factor is also reduced) has little impact on improving the P_d of the device, but the F_{opt} will be increased (Supplementary Fig. S16), increasing the cost of the device. Through further optimization calculations, we can subsequently derive an expression for the maximum P_d at various parts of the human body under the assumption of ideal structural parameters and by neglecting interface thermal resistance (K_c & $K_{con} = 0$):

$$P_d = \frac{Z \cdot (T_b - T_a)^2 \cdot h_s}{4 \cdot (2 + ZT_{avg} + 2\sqrt{1 + ZT_{avg}})} \quad (14)$$

where h_s represents the equivalent skin thermal resistance. For instance, the equivalent skin thermal resistance is relatively low for body parts like the forehead (25–40 $Wm^{-2}K^{-1}$). When K_c & $K_{con} = 0$ and at room temperature, the maximum achievable P_d by a Mg-based w-TEG with a ZT of approximately 0.75 is 67 μWcm^{-2}. Conversely, for body parts with relatively large equivalent skin thermal resistance, such as the foot (7–25 $Wm^{-2}K^{-1}$), the maximum achievable P_d is about 33 μWcm^{-2} (Supplementary Table S4).

Device preparation and mechanical properties

The materials and device structures were chosen based on the results in the previous section. The TE legs are Mg-based materials without tellurium (n-type: $Mg_{3.2}Bi_{1.49}Sb_{0.5}Se_{0.01}$; p-type: $MgAg_{0.95}Sb_{0.99}$). The filler material is polyurethane and the substrate materials are PDMS filled with liquid metal (LM) and copper composites. The fabrication steps are illustrated in the method part. Both the substrate and the filler have excellent stretchability, which can effectively reduce the h_{con}, which is very important for enhancing the performance of wearable heat collection (Supplementary Fig. S17). The stress-strain results of the substrate and the filler are shown in Supplementary Fig. S10. The solid-liquid blend substrate with high thermal conductivity (2.1 $Wm^{-1}K^{-1}$) and low thermal conductivity filler (0.025 $Wm^{-1}K^{-1}$) can reduce the secondary thermal effect, establish a higher temperature difference and improve the output performance of w-TEG (Supplementary Fig. S18). As shown in Fig. 4a, the TE legs of the TEG are connected by S-type copper electrodes, and due to the stretchable encapsulation and electrodes, the prepared device has good flexibility and stretchability (Fig. 4b–d). It can be installed on non-deployable spherical surfaces with a radius of 30 mm or on complex human skin surfaces. The mechanical reliability of w-TEG was demonstrated by measuring the properties under different bending and tensile conditions. Figure 4e illustrates the variation in the w-TEG's resistance over multiple bending cycles, and the results show that the bending radius of the w-TEG can reach 5 mm. When the device was placed on a testing platform with a target bending radius of 10 mm, its internal resistance change rate (R_{TEG_0}/R_{TEG}) and output remained relatively stable throughout more than 500 bending cycles (Fig. 4f, g). In addition, our w-TEG showed up to 30% stretchability, and the R_{TEG_0}/R_{TEG} and output performance of the device remained unchanged after more than 200 repetitions at 20% strain (Fig. 4h–j).

https://doi.org/10.1038/s41467-024-52841-1

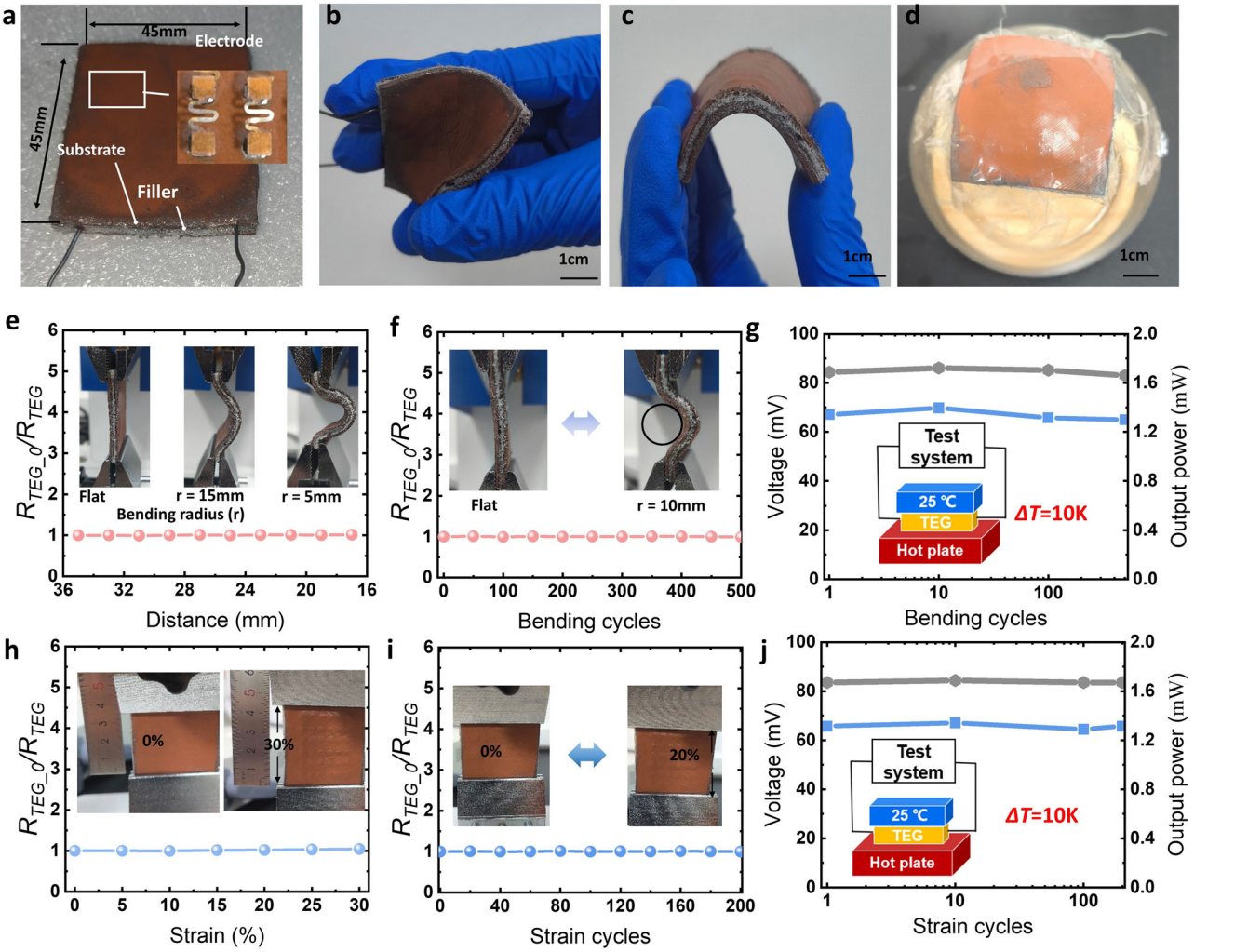

Fig. 4 | Photographs and mechanical properties of w-TEG. a–d Photographs of a fabricated w-TEG and its bending performance, respectively. Variation in R_{TEG0}/R_{TEG} of the w-TEG as a function of (**e**), Bending radius, and (**f**), Bending cycles. **g** Voltage and output power of the w-TEG as a function of bending cycles when $\Delta T = 10$ K. Variation in R_{TEG0}/R_{TEG} of the w-TEG as a function of (**h**), Strain and (**i**), Strain cycles. **j** Voltage and output power of the w-TEG as a function of strain cycles when $\Delta T = 10$ K.

Model verification

To validate the accuracy of the model discussed above, we fabricated w-TEGs with different structures and conducted several verification tests on the fabricated devices to confirm the reliability of the model. We set up a test system for TE performance (Fig. 5a) and a test system for mechanical performance (Fig. 5b). First of all, w-TEGs with leg heights of 2.5–4 mm and F values of 3–17% were separately placed on an arm and subjected to three different heat transfer conditions (natural convection, moderate convective heat transfer, and higher convective heat transfer). Results from 1D numerical analysis, FEA, and experimental characterization are shown in Fig. 5c–e. The experimental results are in good agreement with the predicted results but slightly deviate under the conditions of low F or high convection. The reasons could be accounted for w-TEGs with low F have a greater influence on secondary thermal effects (FEA also proves this result). The results under high convection conditions were higher than expected because the device not only collects heat from the skin it covers, but the surrounding skin also supplements heat to the hot end of the device, and the skin slightly alters its metabolism (heat production) as the environment becomes cold/hot. The second set of verification tests focused on T_s. Similar to the first set of tests, devices were separately placed on an arm under the same three heat dissipation conditions, and the experimentally obtained T_s values on the arm were found to align closely with those anticipated from the model, as shown in Fig. 5f. The third set of verification tests addressed mechanical performance. Devices with optimized F and three different L values were each placed beneath a cylindrical object to exert pressure. The applied pressure and the bending radius of the w-TEG on the cylinder were recorded, from which experimental Ei_{TEG} results were derived for comparison with the numerical model (Fig. 5g). The high level of conformity between the expected values and the experimental results highlights the reliability and sophistication of our model.

w-TEG performance during operation on a human body

A Mg-based w-TEG with an area of 4.5 cm × 4.5 cm was fabricated based on the design criteria discussed above to validate the efficiency and reliability of our model and design procedure for practical applications. First, a composite SiO_2/TiO_2/PMDS (STP) radiative cooling (RC) film was applied to the device (Fig. 6a) to enhance the heat exchange between the device and the environment[48]. The ultraviolet (UV) reflectance and infrared emissivity characteristics of the composite film are presented in Supplementary Fig. S19, which shows that it exhibits both high UV reflectance and high infrared emissivity to meet the heat exchange requirements. We subsequently evaluated the device's voltage on a human wrist (Fig. 6b) and thigh (Fig. 6c). Compared to the wrist, the open circuit voltage of the thigh is lower, and

https://doi.org/10.1038/s41467-024-52841-1

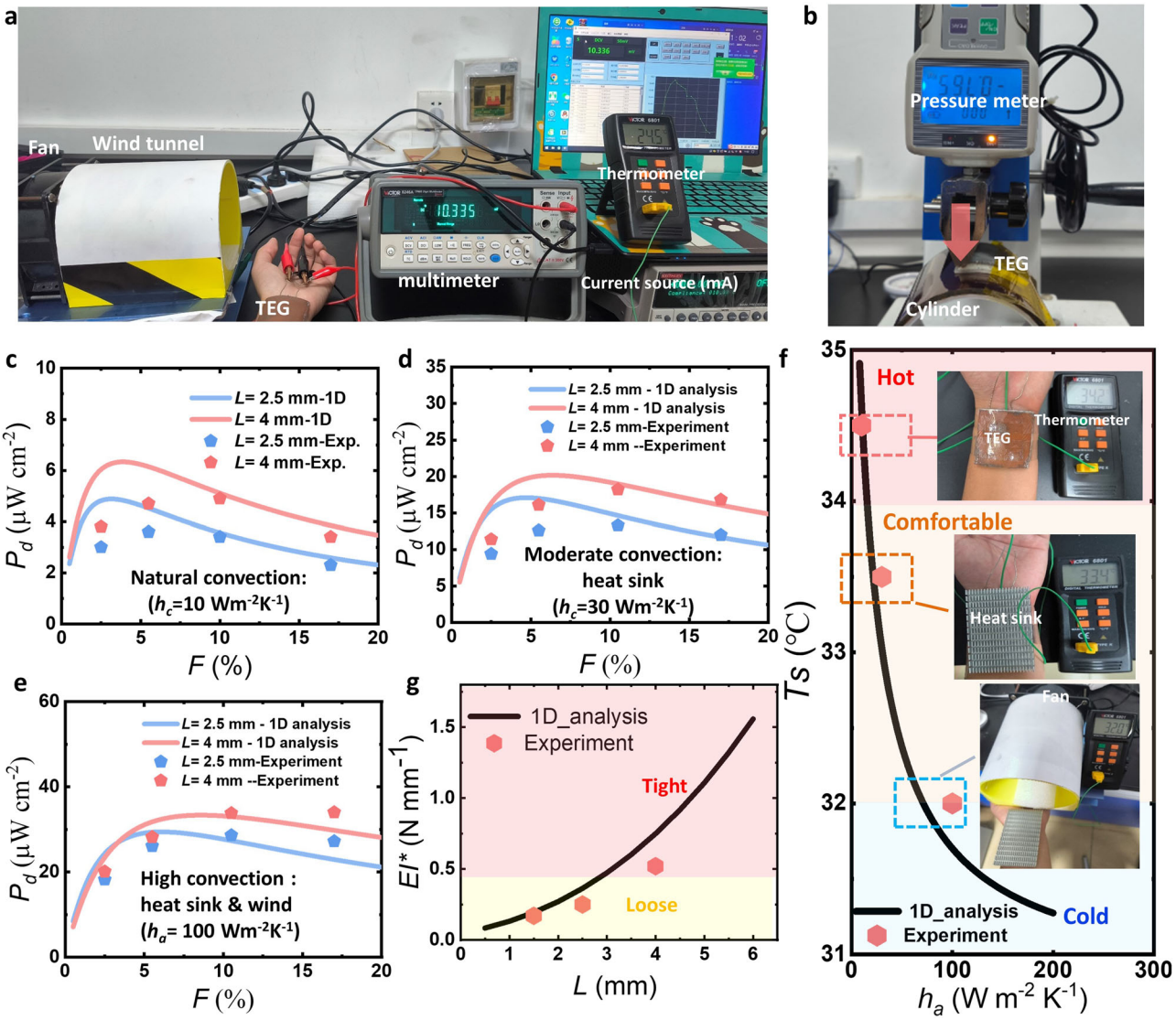

Fig. 5 | Model verification. Testing platform (**a**), For determining simulated P_d, T_s at different L, F, h_a values for experimental validation of the model, and (**b**), For determining simulated Ei_{TEG} at different L values for experimental validation of the model. Simulation-based (**c**–**e**),P_d and (**f**) T_s under different h_a for experimental validation of the model. **g** Comparison of experimental Ei_{TEG} results with those from calculations.

the voltage of the device reaches thermal equilibrium and becomes stable after 5 mins, at which time the output power of the device worn on the arm was obtained. The results (Fig. 6d) revealed that at room temperature, the w-TEG exhibited an output power of up to 126 μW when the person wearing the device stood still, while its output power reached 367 μW (P_d = 18.4 μWcm^{-2}) when the wearer engaged in slow walking (walking speed = 1 ms^{-1}). Furthermore, when a temperature difference of 40 K was applied, the device achieved a maximum P_d of 0.9 mWcm^{-2} (Supplementary Fig. S20). This Mg-based w-TEG with meticulously optimized geometry thus exhibited output and flexibility comparable to those of Bi_2Te_3-based devices. Demonstrations of body-heat harvesting showed that our w-TEG can be widely employed for sustainably powering microwatt-scale wearable electronic devices (Fig. 6e). Figure 6f provides a comprehensive comparison between our Mg-based w-TEG and state-of-the-art Bi_2Te_3-based devices in terms of P_d, ZT of the TE materials, Bending curvature (r^{-1}), flexibility (Ei_{TEG}^{-1}), and T_s. It is evident that our work (indicated by the red pentagon and stars) excels in all these aspects[13,21,22,26,49–54], indicating the exceptional overall performance of our device. Finally, this design strategy is also suitable for other TE materials, such as Bi_2Te_3, or low-temperature industrial applications that do not need to consider wearability. For example, we used this design strategy to collect the heat from hot water at 50 °C (or industrial wastewater) and successfully drive a Bluetooth thermometer to remotely monitor the ambient temperature (Supplementary note S7). The design process of object-oriented w-TEG is summarized in Supplementary Note S8. In this work, a system design strategy proposed by us will have a positive effect on the field of thermoelectric devices.

Discussion

In conclusion, for practical applications, an ideal wearable thermoelectric generator (w-TEG) should not only fulfill power generation requirements but its wearability should also be comprehensively considered. We calculated the output performance of the w-TEG system, including power and voltage, as well as aspects of wearing comfort such as bending radius, bending pressure, skin temperature, and other multidimensional parameters, providing a connection between the device and the human body based on an analytical model. Through decoupled analysis, we proposed a set of system-level design strategies for the rapid assessment of maximum output power and optimal

https://doi.org/10.1038/s41467-024-52841-1

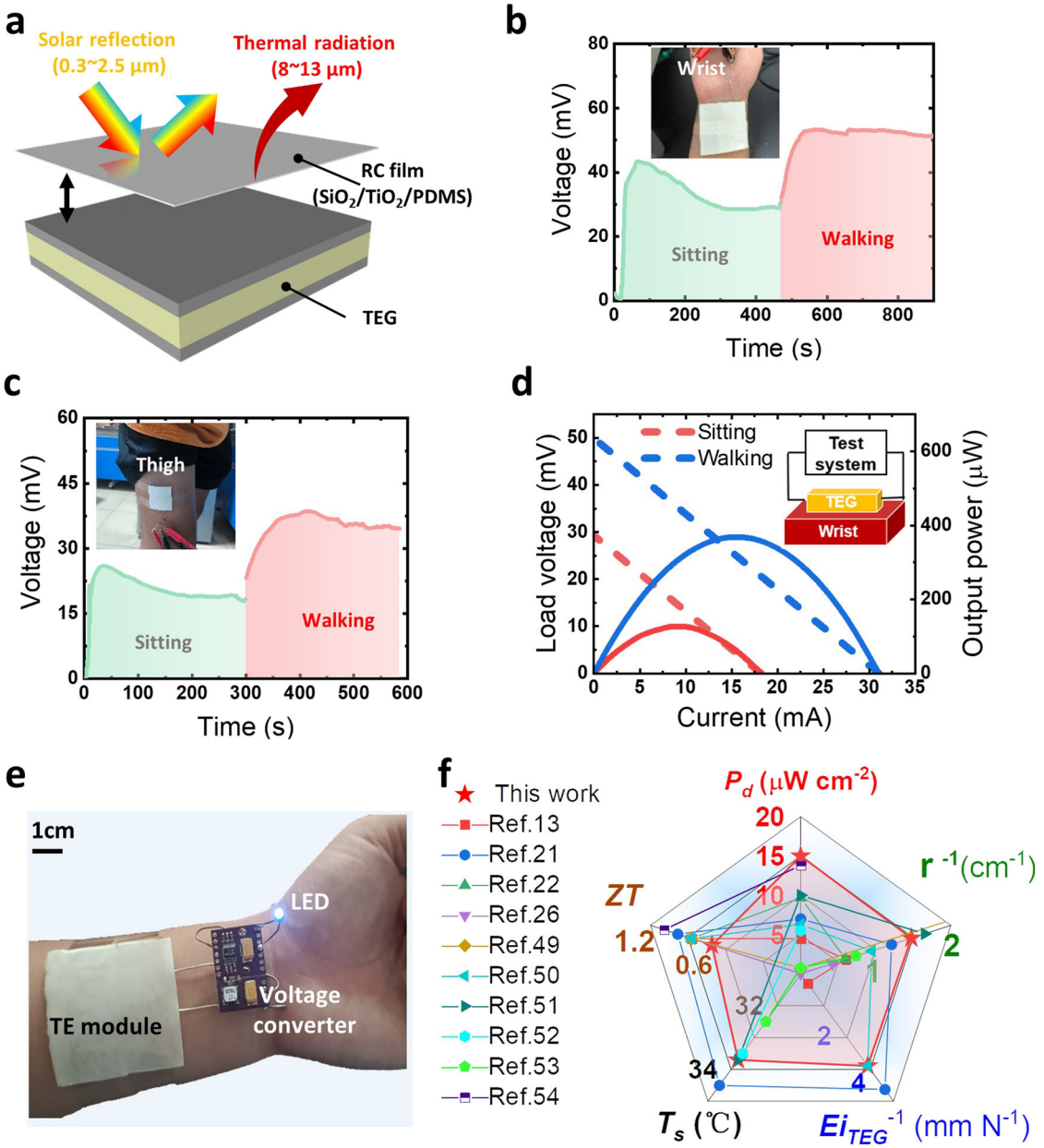

Fig. 6 | Design and application of a Mg-based w-TEG. a Schematic illustration of the Mg-based w-TEG structure enhanced with radiative cooling for improved heat exchange. Measured open-circuit voltages of the w-TEG (**b**) When worn on the arm and (**c**) When worn on the thigh. **d** Testing of the w-TEG's power generation performance [load voltage (dashed curves) and output power (solid curves) as functions of current] when worn on the wrist. **e** Photograph of a w-TEG driven by body heat collection powering a light-emitting diode (LED) through a voltage converter. **f** Comprehensive comparison between this study and previously reported state-of-the-art Bi_2Te_3-based w-TEGs.

wearability for w-TEGs. Following this approach, we developed a high-power-density Mg-based w-TEG that exhibits excellent flexibility and wearer comfort. The research findings underscore the effectiveness of our w-TEG in harvesting body heat for energy, with potential applications extending to self-powered wearable electronic devices and sensors. This work provides an in-depth perspective on the system-level design of wearable thermoelectric systems and low-temperature-difference thermoelectric cogeneration systems.

Methods

Synthesis and preparation of n-type Mg_3Bi_2-based TE material

Magnesium (Mg) powder (99.5%, Aladdin), bismuth (Bi) powder (99.99%, Aladdin), antimony (Sb) powder (99.5%, Aladdin), and selenium (Se) powder (99.5%, Aladdin) were weighed inside a glove box according to the nominal composition $Mg_{3.2}Bi_{1.49}Sb_{0.5}Se_{0.01}$. The raw materials were then loaded into a stainless steel can and continuously ball-milled at 550 rpm (SPEX 8000 M) for 20 h in an argon (Ar) environment. The ball-to-powder weight ratio was approximately 30:1. After the ball-milling process was complete, the powdered material obtained was removed from the glove box and placed in an agate mortar for further grinding. The ground powder was then compacted uniformly and sandwiched between two layers of 304 stainless steel powder inside a graphite mold with a diameter of 12.7 mm (the upper and lower barrier layers were approximately 0.5 mm each, and the TE material had a height of ~2.5 mm). Spark plasma sintering (SPS) was performed under pressure of 60 MPa with a

heating rate of 100 K min^{-1} to reach 773 K, which was maintained for 5 min, followed by additional heating at a rate of 100 K min^{-1} to reach 1073 K for sintering for 5 mins.

Synthesis and preparation of p-type MgAgSb-based TE material

Mg powder (99.5%, Aladdin), silver (Ag) powder (99.9%, Macklin), and Sb powder (99.5%, Aladdin) were weighed inside a glove box according to the nominal composition $MgAg_{0.95}Sb_{0.99}$ and placed in a ball milling can. The mixture was then ball-milled for 18 h under an Ar atmosphere at a rotational speed of 600 rpm. The obtained powder was compacted between two layers of Ag powder and placed into a graphite mold with a diameter of 12.7 mm (the upper and lower barrier layers were ~ 0.75 mm each, and the TE material had a height of ~ 2.5 mm) for SPS. Sintering was carried out under pressure of 60 MPa, and the temperature was raised to 523 K at a rate of 150 K min^{-1}, followed by slow heating at a rate of 50 K min^{-1} to reach 573 K, which was maintained for 10 mins. The sintered samples were then subjected to a heat treatment at 573 K for 10 days in a tubular furnace with a mixed gas atmosphere containing 5% H_2 and 95% Ar.

Substrate precursor

The stretchable substrate precursor was prepared by mixing PDMS (10 wt%-diluent, used to reduce viscosity), GaIn (75.5 wt% Ga and 24.5 wt% In), and copper (10 μm, Aladdin) in a ratio of 35 vol%: 50 vol%: 15 vol%. After adding LM and stirring for 30 mins (oxidizing LM to prevent copper corrosion), add copper and stir for 30 mins.

Synthesis of radiative cooling film

To prepare the composite SiO_2/TiO_2/PMDS (STP) radiative cooling (RC) film, inorganic particles of SiO_2 (5 μm, Aladdin) and TiO_2 (150 nm, Aladdin) were first added to a reagent bottle containing ethyl acetate (99.9%, Aladdin) and sealed. The mixture was stirred using a magnetic stirrer at room temperature with a rotational speed of 1000 rpm for 1 h to obtain a well-dispersed SiO_2/TiO_2 suspension. PDMS (Sylgard 184, Dow Corning) was then added in a mass ratio of 10:1 to the prepared SiO_2/TiO_2 suspension. The mixture was stirred using a magnetic stirrer at room temperature with a rotational speed of 1000 rpm for an additional hour. Ultrasonic dispersion was subsequently performed for 20 mins. After completion of the ultrasonic treatment, a curing agent was added to the PDMS mixture in a mass ratio of 10:1, and the mixture was mixed at room temperature for 10 mins to obtain the STP composite solution. The prepared STP coating solution was degassed for 3 mins in a 100% ultrasonic cleaner to obtain the coating solution, which was poured onto an aluminum foil fixed reflector surface and spread into a film using a film coater. Finally, the coated sample was placed in an oven for heating with a staged profile. The temperature was initially maintained at 40 °C for 30 mins and then gradually raised to 60 °C, which was maintained for 2 h to obtain an RC composite film with a smooth and uniform surface without bubbles. For practical human body energy harvesting applications, the RC film is attached to the top of the device to enhance heat exchange between the device and the environment.

w-TEG fabrication steps

Step 1: The bulk TE materials prepared as described above were cut into n-type Mg_3Bi_2-based TE legs with dimensions of 1.5 mm × 1.5 mm × 3.5 mm and p-type MgAgSb-based TE legs with dimensions of 2 mm × 2 mm × 3.5 mm.

Step 2: Copper electrodes were prepared using the transfer etching method and then coated with a 0.2 mm-thick layer of solder paste using screen printing. The prepared TE legs were placed onto the solder-paste-coated copper electrodes and placed on a heating stage. The temperature was raised to 240 °C and maintained for 30 s.

Step 3: In a mold, the substrate precursor prepared as described above was poured to a thickness of about 1–1.5 mm and preheated at 80 °C for 10 mins. At this point, the surface of this hard substrate layer had not yet solidified. The device prepared in Step 2 was then placed on this preheated layer, and an additional layer of PDMS with a thickness of about 0.2 mm was poured. The assembly was then placed on the heating stage and heated to 80 °C for 1 h. The same procedure was used to encapsulate the top electrode using the top substrate prepared as described above.

Step 4: A polyurethane precursor (1076a) and a catalyst (1076b) were mixed in a weight ratio of 2.5:1 and stirred for about 10 s. The mixture was quickly drawn into a syringe and injected between the TE legs. The polyurethane subsequently foamed in the air and naturally solidified to form the structure.

The w-TEG fabrication steps are schematically illustrated in Supplementary Fig. S25.

Material characterization

The electrical conductivity (σ) and Seebeck coefficient (α) of all materials were measured using the ZEM-3 apparatus (ULVAC, Japan). The tested samples were cut and polished to form rectangular specimens with dimensions of 3 mm × 3 mm × 12.5 mm. The testing temperature ranged from 323 K to 523 K, with a temperature gradient set at 50 K.

The thermal conductivity (κ) of the TE materials was calculated using the formula: $\kappa = D_{TE}C_P d$, where D_{TE} represents the thermal diffusivity of TE material, C_P is the specific heat capacity of the material, and d is the material density. Given that measuring C_P introduces significant measurement error, previously reported values were adopted. In this study, previously reported C_P values for n-type Mg_3Bi_2-based TE materials[41,55], determined using the Archimedes drainage method, were used. D_{TE} was measured using the LFA 457 laser thermal analyzer (NETZSCH, Germany). The κ values of the filling and substrate materials were measured using a thermal conductivity analyzer (TCi, C-Therm Technologies Ltd.)

Contact resistance testing was conducted using a homemade four-probe measurement apparatus. The testing current was set at 100 mA. As the probes moved from the contact metal layer through the contact interface to the TE material, a series of voltage readings were recorded to calculate the contact resistance.

Thermoelectric and mechanical performance characterization of w-TEGs

The P_d of each device was characterized using a digital multimeter (Victor, VC8246A) to measure the load voltage (V_l) of the w-TEG. The P_d was deduced using the formula $P_d = \frac{V_l^2}{R_l * A}$, where R_l is the resistance of the load resistor and A denotes the device area. During testing under walking conditions, a fan was placed at the top of the device to simulate an airspeed of 1.5 ms^{-1}. The airflow speed was measured using an airflow velocity sensor (SMART SENSOR, AS836). The internal resistance of the w-TEG after bending was determined by calculating the slope of the I-V curve, which was established by subjecting the w-TEG to a range of currents from − 30 mA to 30 mA using a source meter (Tektronix Keithley 6220) while simultaneously measuring the voltage difference.

Three-dimensional finite element analysis of w-TEG performance

We employed COMSOL Multiphysics (COMSOL Inc.) coupled with the Heat Transfer and Electric Current modules to assess the thermoelectric performance of our w-TEG. Within the TE module, the π-shaped TE legs were enveloped by the filling material and connected to copper foil electrodes. These electrodes were further encapsulated by the thermal conductive substrates. The model dimensions and boundary conditions for the specific w-TEG configuration used in the simulation are illustrated in Supplementary Fig. S8c. Simulation parameters included the material properties provided in Supplementary

Table S3, as well as default values available within the COMSOL Multiphysics software package.

Reporting Summary

Further information on research design is available in the Nature Portfolio Reporting Summary linked to this article.

Data availability

The data supporting the plots in this paper and the other findings of this study are available from the corresponding author upon reasonable request.

References

1. Gao, W., Ota, H., Kiriya, D., Takei, K. & Javey, A. Flexible electronics toward wearable sensing. *Acc. Chem. Res.* **52**, 523–533 (2019).
2. Petsagkourakis, I. et al. Thermoelectric materials and applications for energy harvesting power generation. *Sci. Tech. Adv. Mater.* **19**, 836–862 (2018).
3. Jia, Y. et al. Wearable thermoelectric materials and devices for self-powered electronic systems. *Adv. Mater.* **33**, 202102990 (2021).
4. Ryu, H., Yoon, H. J. & Kim, S. W. Hybrid energy harvesters: toward sustainable energy harvesting. *Adv. Mater.* **31**, 201802898 (2019).
5. Zhu, S. et al. Review on wearable thermoelectric generators: from devices to applications. *Energies* **15**, 3375 (2022).
6. Lee, B. et al. High-performance compliant thermoelectric generators with magnetically self-assembled soft heat conductors for self-powered wearable electronics. *Nat. Commun.* **11**, 5948 (2020).
7. Bahk, J.-H., Fang, H., Yazawa, K. & Shakouri, A. Flexible thermoelectric materials and device optimization for wearable energy harvesting. *J. Mater. Chem. C* **3**, 10362–10374 (2015).
8. Cao, T., Shi, X.-L. & Chen, Z.-G. Advances in the design and assembly of flexible thermoelectric device. *Prog. Mater. Sci.* **131**, 101003 (2023).
9. Nozariasbmarz, A. et al. Review of wearable thermoelectric energy harvesting: from body temperature to electronic systems. *Appl. Energy* **258**, 114069 (2020).
10. He, J. & Tritt, T. M. Advances in thermoelectric materials research: looking back and moving forward. *Science* **357**, 1369 (2017).
11. Kim, D.-H., Ghaffari, R., Lu, N. & Rogers, J. A. Flexible and stretchable electronics for biointegrated devices. *Annu. Rev. Biomed. Eng.* **14**, 113–128 (2012).
12. Yang, Y. et al. Stretchable nanolayered thermoelectric energy harvester on complex and dynamic surfaces. *Nano Lett.* **20**, 4445–4453 (2020).
13. Fan, W. et al. High-performance stretchable thermoelectric generator for self-powered wearable electronics. *Adv. Sci.* **10**, 202206397 (2023).
14. Kim, C. S. et al. Self-powered wearable electrocardiography using a wearable thermoelectric power generator. *ACS Energy Lett.* **3**, 501–507 (2018).
15. Liu, Y. et al. A wearable real-time power supply with a Mg_3Bi_2-based thermoelectric module. *Cell Rep. Phys. Sci.* **2**, 100412 (2021).
16. Xu, Q. et al. High-performance, flexible thermoelectric generator based on bulk materials. *Cell Rep. Phys. Sci.* **3**, 100780 (2022).
17. Lv, J.-R., Ma, J.-L., Dai, L., Yin, T. & He, Z.-Z. A high-performance wearable thermoelectric generator with comprehensive optimization of thermal resistance and voltage boosting conversion. *Appl. Energy* **312**, 118696 (2022).
18. Liu, W. et al. A liquid metal-Enhanced wearable thermoelectric generator. *Bioengineering* **9**, 9060254 (2022).
19. Soleimani, Z., Zoras, S., Ceranic, B., Cui, Y. & Shahzad, S. A comprehensive review on the output voltage/power of wearable thermoelectric generators concerning their geometry and thermoelectric materials. *Nano Energy* **89**, 106325 (2021).
20. Hasan, M. N., Nafea, M., Nayan, N. & Mohamed Ali, M. S. Thermoelectric generator: materials and applications in wearable health monitoring densors and internet of things devices. *Adv. Mater. Technol.* **7**, 2101203 (2021).
21. Hong, S. et al. Wearable thermoelectrics for personalized thermoregulation. *Sci. Adv.* **5**, eaaw0536 (2019).
22. Wei, H., Zhang, J., Han, Y. & Xu, D. Soft-covered wearable thermoelectric device for body heat harvesting and on-skin cooling. *Appl. Energy* **326**, 119941 (2022).
23. Zhu, P. et al. A self-healable, recyclable, and flexible thermoelectric device for wearable energy harvesting and personal thermal management. *Energy Convers. Manag.* **285**, 117017 (2023).
24. Liu, Z. et al. Demonstration of ultrahigh thermoelectric efficiency of ~7.3% in Mg_3Sb_2/MgAgSb module for low-temperature energy harvesting. *Joule* **5**, 1196–1208 (2021).
25. Liang, J. S. et al. Synergistic effect of band and nanostructure engineering on the boosted thermoelectric performance of n-Type $Mg_{3+\delta}$ (Sb, Bi)$_2$Zintls. *Adv. Energy Mater.* **12**, 202201086 (2022).
26. Hu, K. et al. Optimized thermal design for excellent wearable thermoelectric generator. *J. Mater. Chem. A* **10**, 24985–24994 (2022).
27. Montecucco, A. & Knox, A. R. Accurate simulation of thermoelectric power generating systems. *Appl. Energy* **118**, 166–172 (2014).
28. Astrain, D., Vián, J. G., Martínez, A. & Rodríguez, A. Study of the influence of heat exchangers' thermal resistances on a thermoelectric generation system. *Energy* **35**, 602–610 (2010).
29. Eldesoukey, A. & Hassan, H. 3D model of thermoelectric generator (TEG) case study: effect of flow regime on the TEG performance. *Energy Convers. Manag.* **180**, 231–239 (2019).
30. Zhu, K. et al. System efficiency and power: the bridge between the device and system of a thermoelectric power generator. *Energy Environ. Sci.* **13**, 3514–3526 (2020).
31. Kishore, R. A., Nozariasbmarz, A., Poudel, B., Sanghadasa, M. & Priya, S. Ultra-high performance wearable thermoelectric coolers with less materials. *Nat. Commun.* **10**, 1765 (2019).
32. Xing, Y. et al. High-performance wearable Bi_2Te_3-based thermoelectric generator. *Appl. Sci.* **13**, 5971 (2023).
33. Lee, Y. G. et al. Design and experimental investigation of thermoelectric generators for wearable applications. *Adv. Mater. Technol.* **2**, 1600292 (2017).
34. Leonov, V. & Vullers, R. J. M. Wearable thermoelectric generators for body-powered devices. *J. Electron. Mater.* **38**, 1491–1498 (2009).
35. Suarez, F., Nozariasbmarz, A., Vashaee, D. & Öztürk, M. C. Designing thermoelectric generators for self-powered wearable electronics. *Energy Environ. Sci.* **9**, 2099–2113 (2016).
36. Webb, P. Temperatures of skin, subcutaneous tissue, muscle and core in resting men in cold, comfortable and hot conditions. *Appl. Phycol.* **64**, 471–476 (1992).
37. Leonov, V., Torfs, T., Fiorini, P. & Van Hoof, C. Thermoelectric converters of human warmth for self-powered wireless sensor nodes. *IEEE Sens. J.* **7**, 650–657 (2007).
38. Zhao, W. et al. Superparamagnetic enhancement of thermoelectric performance. *Nature* **549**, 247–251 (2017).
39. Hinterleitner, B. et al. Thermoelectric performance of a metastable thin-film heusler alloy. *Nature* **576**, 85–90 (2019).
40. Ying, P. et al. A robust thermoelectric module based on MgAgSb/Mg_3(Sb,Bi)$_2$with a conversion efficiency of 8.5% and a maximum cooling of 72 K. *Energy Environ. Sci.* **15**, 2557–2566 (2022).
41. Liu, Z. et al. Maximizing the performance of n-type Mg_3Bi_2 based materials for room-temperature power generation and thermoelectric cooling. *Nat. Commun.* **13**, 1120 (2022).
42. Bu, Z. et al. A record thermoelectric efficiency in tellurium-free modules for low-grade waste heat recovery. *Nat. Commun.* **13**, 237 (2022).

43. Zheng, Y. et al. Extraordinary thermoelectric performance in MgAgSb alloy with ultralow thermal conductivity. *Nano Energy* **59**, 311–320 (2019).
44. Mori, Y., Kioka, E. & Tokura, H. Effects of pressure on the skin exerted by clothing on responses of urinary catecholamines and cortisol, heart rate and nocturnal urinary melatonin in humans. *Int. J. Biometeorol.* **47**, 1–5 (2002).
45. Saggin, B., Tarabini, M. & Lanfranchi, G. A device for the skin–contact thermal resistance measurement. *IEEE Trans. Instrum. Meas.* **61**, 489–495 (2012).
46. Ho, H. N. & Jones, L. A. Thermal model for hand-object interactions. *Symposium on Haptics Interfaces for Virtual Environment and Teleoperator Systems 2006, Proceedings*, 461–467 (2006).
47. Nozariasbmarz, A. et al. Thermoelectric generators for wearable body heat harvesting: Material and device concurrent optimization. *Nano Energy* **67**, 104265 (2020).
48. Sun, Y. et al. Design and preparation of flexible double-layered daytime radiative cooling composite film with antifouling property. *Sol. Energy Mater. Sol. Cells* **245**, 111836 (2022).
49. Zhu, S. et al. Simultaneous realization of flexibility and ultrahigh normalized power density in a heatsink-free thermoelectric generator via fine thermal regulation. *ACS Appl. Mater. Interfaces* **14**, 1045–1055 (2022).
50. Wang, Y. et al. High-performance stretchable organic thermoelectric generator via rational thermal interface design for wearable electronics. *Adv. Energy Mater.* **12**, 2102835 (2021).
51. Jo, S. E., Kim, M. K., Kim, M. S. & Kim, Y. J. Flexible thermoelectric generator for human body heat energy harvesting. *Electron. Lett.* **48**, 1015–1017 (2012).
52. Kim, S. J., We, J. H. & Cho, B. J. A wearable thermoelectric generator fabricated on a glass fabric. *Energy Environ. Sci.* **7**, 1959–1965 (2014).
53. Jung, S.-J. et al. Porous organic filler for high efficiency of flexible thermoelectric generator. *Nano Energy* **81**, 105604 (2021).
54. Liu, Y. et al. Passive radiative cooling enables improved performance in wearable thermoelectric generators. *Small* **18**, 202106875 (2022).
55. Mo, X. et al. High thermoelectric performance at room temperature of n-type Mg_3Bi_2-based materials by Se doping. *J. Magnes. Alloy.* **10**, 1024–1032 (2022).

Acknowledgements

L.M., J.G., and P.Y. gratefully acknowledge financial support from the National Natural Science Foundation of China (Grant No. U21A2054 and 52273285), J.G. gratefully acknowledges financial support from National Natural Science Foundation of China (Grant No.51961011), Y. P. gratefully acknowledges financial support from National Natural Science Foundation of China (Grant No.52262032). T.M. acknowledges support from JST Mirai JPMJMI19A1.

Author contributions

L.M. and S.Z. conceived the idea, prepared the devices, and wrote the draft. Y.G., J.C., and Z.Z. assisted in measuring the properties of devices. J. L. assisted in TE materials synthesis and simulation analysis. J. G., Y. P., and C. L. assisted in editing the manuscript. L.M. and T.M. supervised this research and revised the manuscript as corresponding authors. All authors contributed to the interpretation of the data and to the writing of the manuscript.

Competing interests

L. Miao, S. Zhu, C. Liu, J. Gao, and Y. Gao have applied for two Chinese patents (ZL202010977167.9, 202211728686.7) on the main parts of w-TEG described here. The remaining authors declare no competing interests.

Additional information

Supplementary information The online version contains supplementary material available at https://doi.org/10.1038/s41467-024-52841-1.

Correspondence and requests for materials should be addressed to Lei Miao or Takao Mori.

Peer review information *Nature Communications* thanks Yuanwen Gao, Jian-Wei Liu, and the other anonymous reviewer(s) for their contribution to the peer review of this work. A peer review file is available.